Astronomy & Astrophysics manuscript no. 0051main
February 20, 2024
© ESO 2024

arXiv:0809.0317v1 [astro-ph] 1 Sep 2008

Atomic diffusion and mixing in old stars

II. Observations of stars in the globular cluster NGC 6397 with VLT/FLAMES-GIRAFFE ⋆

K. Lind[1,2], A. J. Korn[1], P. S. Barklem[1], and F. Grundahl[3]

[1] Department of Physics & Astronomy, Uppsala University, Box 515, 751 20 Uppsala, Sweden
[2] European Southern Observatory (ESO), Karl-Schwarzschild-Strasse 2, 857 48 Garching bei München, Germany
e-mail: klind@eso.org
[3] Department of Physics & Astronomy, University of Aarhus, Ny Munkegade, 8000 Aarhus C, Denmark

Received 25/04/2008; accepted 25/08/2008

ABSTRACT

Context. Evolutionary trends in the surface abundances of heavier elements have recently been identified in the globular cluster NGC 6397 ([Fe/H]= −2), indicating the operation of atomic diffusion in these stars. Such trends constitute important constraints for the extent to which diffusion modifies the internal structure and surface abundances of solar-type, metal-poor stars.
Aims. We perform an independent check of the reality and size of abundance variations within this metal-poor globular cluster.
Methods. Observational data covering a large stellar sample, located between the cluster turn-off point and the base of the red giant branch, are homogeneously analysed. The spectroscopic data were obtained with the medium-high resolution spectrograph FLAMES/GIRAFFE on VLT-UT2 ($R \sim 27\,000$). We derive independent effective-temperature scales from profile fitting of Balmer lines and by applying colour-$T_{\rm eff}$ calibrations to Strömgren *uvby* and broad-band *BVI* photometry. An automated spectral analysis code is used together with a grid of MARCS model atmospheres to derive stellar surface abundances of Mg, Ca, Ti, and Fe.
Results. We identify systematically higher iron abundances for more evolved stars. The turn-off point stars are found to have 0.13 dex lower surface abundances of iron compared to the coolest, most evolved stars in our sample. There is a strong indication of a similar trend in magnesium, whereas calcium and titanium abundances are more homogeneous. Within reasonable error limits, the obtained abundance trends are in agreement with the predictions of stellar structure models including diffusive processes (sedimentation, levitation), if additional turbulent mixing below the outer convection zone is included.

Key words. Stars: abundances – Stars: Population II – Globular clusters: general – Techniques: spectroscopic – Methods: observational – Diffusion

1. Introduction

A globular cluster (GC) constitutes, in many respects, a homogeneous stellar population and is therefore an excellent laboratory for testing and constraining models of stellar structure and evolution. Chemical abundances inferred from observations of GCs can give important clues to the physical processes at work in individual stars. Recently a discovery was made pointing to the existence of systematic differences in surface abundances between stars in different evolutionary stages in a metal-poor GC. Korn et al. (2007) (hereafter Paper I) observe four samples of stars located between the main sequence (MS) turn-off (TO) point and the red giant branch (RGB) of NGC 6397, using FLAMES/UVES on the VLT, and found significant variations in abundances with effective temperature and surface gravity. In particular, they conclude iron to be under-abundant by 0.16 ± 0.05 dex in the atmospheres of the TO stars compared to the RGB stars in their sample. Proposed as an explanation to this phenomenon is a continuous, long-term depletion of iron and other heavy elements from the surface layers, at work during the stars' life-time on the MS. The mechanism responsible for the depletion is generally referred to as atomic diffusion – an umbrella term accounting for several diffusive processes. High ages and thin convective envelopes are factors that make metal-poor TO stars particularly prone to atomic diffusion. Once a star leaves the MS and begins to develop into the giant stage, its outer convection zone gradually reaches deeper layers, and elements that had previously been drained from the surface layers are mixed up again, eventually restoring the initial chemical composition (with fragile elements such as Li as notable exceptions). This is predicted to result in a gradual rise in the surface abundances of the depleted elements as the star evolves along the subgiant and red giant branches (hereafter, we write SGB for subgiant branch). GC stars presumably share the same original composition of elements such as iron, titanium, and calcium, which in combination with their high ages and low metal content make them suitable test cases for stellar structure models including atomic diffusion.

The abundance trend for iron presented in Paper I is directly contradictory to result by Gratton et al. (2001), who by studying TO vs. base-RGB (bRGB) stars conclude that there are no significant difference in iron abundance between the groups (magnesium is, however, found to be 0.15 dex less abundant in the TO stars). The cause for the differing result is twofold: lower effective temperatures are found for the TO stars in Paper I and the analysis include stars on the RGB.

Here we present a follow-up analysis of spectroscopic data from FLAMES/GIRAFFE collected simultaneously to the

⋆ Based on data collected at European Southern Observatory (ESO), Paranal, Chile, under program ID 075.D-0125(A).

observations presented in Paper I. A large sample of stars, $\approx$ 100, covering the range from the TO to the bRGB is homogeneously analysed, with the aim of further constraining possible variations in surface abundance in the cluster. In particular, we investigate whether the results presented in Paper I are robust for a larger sample of stars, analysed with an independent set of tools. We start by describing the observations and the data-reduction procedure in Sect. 2. Sect. 3 is devoted to the determination of fundamental stellar parameters and a description of the spectrum analysis code. In Sect. 4 we present and discuss our abundance results. Sect. 5 compares predictions from stellar-structure models including atomic diffusion to the abundances we have inferred from observations. In Sect. 6 we summarise our conclusions.

2. Observations and data reduction

2.1. Photometric observations

The target selection for the spectroscopic study is based on Strömgren *uvby* photometry. The photometric observations were collected with the DFOSC instrument on the 1.5 m telescope on La Silla, Chile, in 1997. Additional *BVI* photometric data were obtained in 2005. The UCAC2 catalog at Vizier (Ochsenbein et al. 2000) provides astrometry with a precision of $\sim 0\farcs10$ for individual stars. A full description of the photometric observations and their reduction is given in Paper I and references therein.

We select a sample of 135 stars for spectroscopic analysis, located between the cluster TO point at $V = 16.3$ to the bRGB at $V = 15.2$. Apart from providing the target list, the photometry is also considered in this work in the determination of stellar parameters. Fig. 1 shows a colour-magnitude diagram, V versus $(v - y)$, of the cluster, with the selected stars marked.

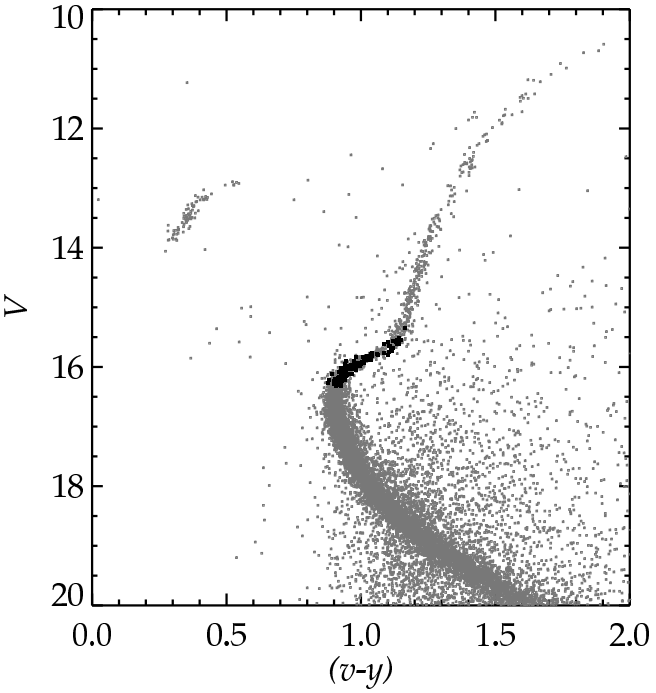


Fig. 1. Observed colour-magnitude diagram of NGC 6397. The targets selected for the spectroscopic study are marked with black squares.

Table 1. Observational setup for FLAMES/GIRAFFE [a].

Setting #	Wavelength range [Å]	Resolution $\lambda/\Delta\lambda$	Exposure time	Dates 2005
5B	4 376 - 4 552	26 000	7h 40m	23,26-29 Mar
7B	4 742 - 4 932	26 700	5h 10m	29-31 Mar
9B	5 143 - 5 356	25 900	3h 50m	01-03 Apr
14B	6 383 - 6 626	28 800	3h 50m	02-04 Apr

[a] Data from http://www.eso.org/instruments/flames

2.2. Spectroscopic observations

All spectroscopic data were collected in Service Mode, with the fibre-fed, multi-object, medium-high resolution spectrograph FLAMES/GIRAFFE (Pasquini et al. 2002) at ESO-VLT. FLAMES allows for 132 objects to be observed simultaneously, with GIRAFFE in MEDUSA mode. A total exposure time of 20.5 h was spent under grey-to-bright lunar conditions, but with good seeing (average seeing $\sim 0.7''$). We apply four of the highest resolution 'B-settings', which together cover a total spectral range of 822 Å in the optical. On average 15 fibres per observation are dedicated to a simultaneous monitoring of the sky background to ensure a proper sky-correction. Stars in different evolutionary stages are distributed randomly across the FLAMES field-of-view. We find no gradient in background light over the field and subtract a single, averaged sky-spectrum from the stellar spectra obtained during each observation. The setup is briefly summarised in Table 1.

Basic reduction of the spectroscopic data is performed with the ESO-maintained GIRAFFE pipeline, version 1.0, using standard settings. Further processing of the data is carried out with MIDAS and C-routines (kindly provided by N. Christlieb). The GIRAFFE CCD chip has a defect in its upper right corner caused by the illumination of a diode, giving elevated dark-current values to a significant number of pixels. If uncorrected for, this will propagate into a flux upturn towards longer wavelengths in dozens of spectra. The feature can be removed by subtracting a dark frame from the raw science frames (after proper scaling with exposure time). To avoid the introduction of additional noise we chose to correct for dark current after the spectra had been extracted, when the glow is a well-behaved and easily smoothable function of wavelength. For this purpose we pseudo-reduce a dark frame produced close in time to the observations. We find, however, that it is necessary to apply an additional, minor scaling factor to the dark counts to completely remove the feature, which we ascribe to the documented time-variability of the glow strength[1].

The radial velocity correction of our stellar spectra results in a cluster mean heliocentric radial velocity of $18.1 \pm 0.3\,\mathrm{km\,s^{-1}}$ from measurements of 133 stars. We find a velocity dispersion of $3.40\,\mathrm{km\,s^{-1}}$. This radial velocity value is in agreement with the recent result by Milone et al. (2006) who derive $18.36 \pm 0.09(\pm 0.10)\,\mathrm{km\,s^{-1}}$ (the first is the random error and the second the systematic error), obtained from 1486 stars. We identify two stars that are not members of the cluster, 502219 and 501856, both with deviating radial velocities and evidently too metal-rich spectra (see Sec. 4).

[1] see the instrument's quality control pages: http://www.eso.org/observing/dfo/quality/GIRAFFE/qc/dark_qc1.html

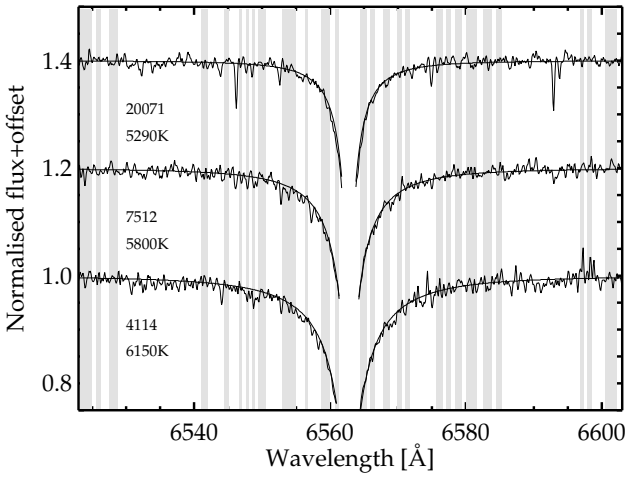


Fig. 2. The best-fit Hα profiles for three stars. The thick line corresponds to a model with the stated effective temperature. The grey-shaded regions represent the regions used for fitting.

After sky-subtraction and radial velocity correction the spectra are coadded and rebinned onto a final wavelength scale with a step size of 0.1 Å. The S/N-ratio of the coadded spectra in the 14B setting varies from 28 to 148 per rebinned pixel with a mean value of 85, estimated from a relatively line-free region between 6 440 -6 449 Å. The corresponding mean value for the bluer 7B setting is 76, from measurements between 4 812 – 4 821 Å.

3. Analysis

In this section we describe how we derive the fundamental parameters necessary to conduct the abundance analysis. We emphasise that we have made an effort to carry out all steps of the investigation using independent tools from those of Paper I, in particular by implementing different spectral synthesis and model atmospheres codes.

3.1. Effective temperatures

Profile fitting of Balmer lines is a well-established $T_{\rm eff}$-indicator in solar-type stars. Considering the reliable flat-fielding which can be obtained with fibre-fed spectroscopy and the large free spectral range of GIRAFFE (FSR ~ 200 Å), this data set is well suited for analysis of broad lines such as the Balmer lines. We implement an automated χ^2-minimization technique for the normalisation and profile fitting of the wings of Hα. Synthetic spectra are produced with the FORTRAN code HLINPROF (Barklem & Piskunov 2003)[2], which is incorporated in the LTE (local thermodynamical equilibrium) spectrum synthesis code SYNTH (Piskunov 1992). We treat Stark broadening according to the tabulated line profiles of Stehlé & Hutcheon (1999) and self broadening (resonance broadening and van der Waals broadening) according to Barklem et al. (2000). Radiative broadening and an estimate of line broadening due to helium collisions are also included in the calculations.

To compute a set of plane-parallel model atmospheres for the spectrum synthesis we use the MARCS code (Gustafsson et al. 1975; Asplund et al. 1997). MARCS is a one-dimensional (1D), LTE model atmospheres code, invoking flux conservation (radiative and convective) and hydrostatic equilibrium. Convection is treated according to the customary mixing length theory, with the mixing length parameters set to $\alpha = 1.5$ and $y = 0.076$.

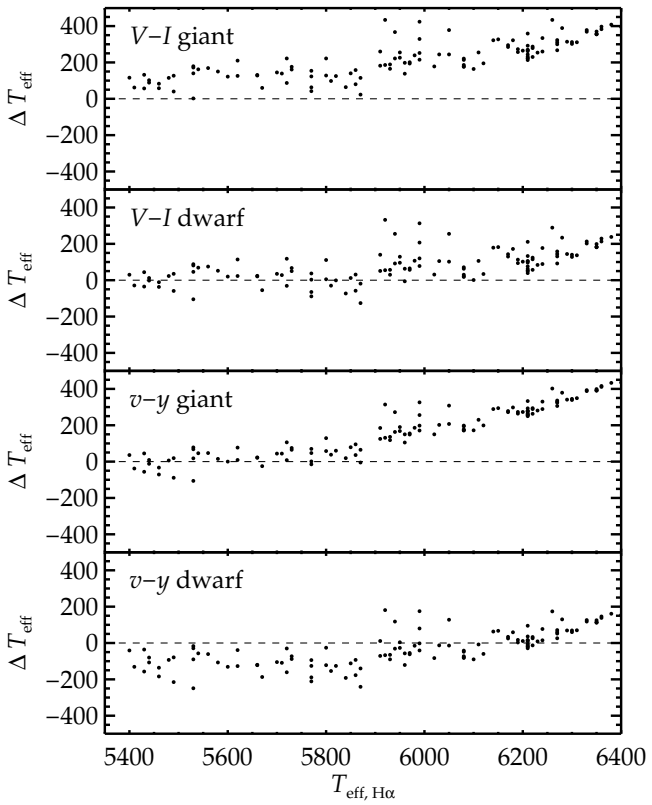


Fig. 3. Comparison between our Hα-based effective temperatures and those obtained by applying the calibrated relations of Alonso et al. (1996, 1999) to colour indices $v - y$ and $V - I$. The y-axis shows $\Delta T_{\rm eff} = T_{\rm eff,H\alpha} - T_{\rm photometry}$ for the stated index and calibration.

The observed spectrum is compared to a grid of synthetic spectra, equidistant in effective temperature with 10 K steps. The fitting only considers regions that are not significantly affected by absorption from metal and telluric lines (see Fig. 2) as judged from high-resolution and high-S/N spectra of metal-poor subgiants. First, an initial guess of the correct model is made and only wavelength regions located ±35 – 50Å from the Hα-line center are used. Here the sensitivity of the hydrogen line to effective temperature is low and the difference between observed and modelled flux is minimised to find the optimal straight line used for normalisation. Thereafter, only wavelength regions in the effective-temperature sensitive parts are used, located within ±25Å of the center, to find the model that minimises the χ^2-distance to the observed flux. However, to avoid modelling uncertainties affecting the line core, only residual flux above 0.75 is considered. The whole procedure is iterated until the initial guess coincides with the resulting $T_{\rm eff}$-value.

By repeatedly adding random noise to synthetic spectra and feeding them as input to the procedure, the precision of the fitting method can be determined. We find that a typical S/N-ratio of 85 gives a random error of about 30 K, for the coolest as well as for the hottest stars. For our lowest-quality spectra the corresponding value is 80 K and for the highest quality data the random error is as low as 15 K. The absolute error in $T_{\rm eff}$ is more difficult to assess, as it depends on several factors in addition

[2] Available at www.astro.uu.se/~barklem.

to observational uncertainty, of which the most important ones are the line broadening of hydrogen, the treatment of convection in the stellar atmosphere, and the stellar parameters $\log g$ and [Fe/H]. Barklem et al. (2002) show that these contributions together may add up to an error of the order of 100 K for stars in this metallicity and effective-temperature range.

From the FLAMES solar atlas[3] we retrieve reduced GIRAFFE spectra from observations illuminating all MEDUSA fibers in the 14B-setting, which we average into a single solar spectrum. Using the setup described above we derive $T_{\rm eff,H\alpha} = 5\,630$ K for the Sun, which is approximately 150 K lower than the accepted value, an offset which we ascribe mainly to observational uncertainty. Barklem et al. (2002) derive a solar effective temperature of $5\,722 \pm 81$ K with the same models, using an Hα-spectrum from the Kitt Peak atlas (Kurucz et al. 1984). The Hα line profile found from the FLAMES/GIRAFFE solar atlas is more narrow compared to e.g. the Kitt peak atlas and we recommend to re-observe the Sun with GIRAFFE with the new CCD (upgraded in May 2008) and seek the reason for this difference.

Using our obtained solar effective temperature as a zero-point offset, we consequently shift all effective temperatures by +150 K. We thus assume that, in the stellar-parameter range spanned by our targets, the Hα-line has a similar sensitivity to effective temperature as the Sun, which may be realistic to a first order approximation. The shifted Hα-based effective temperatures are the ones we later adopt in the abundance analysis and we will refer to them as the spectroscopic $T_{\rm eff}$ in the remaining part of the paper.

To assess the validity of our spectroscopic effective temperatures we construct photometric $T_{\rm eff}$ scales from four different colour indices. The Alonso et al. (1996, 1999) relations, calibrated on the infrared flux method, are used to derive effective temperatures based on $b-y$, $v-y$, $B-V$, and $V-I$. Note that, at this metallicity and stellar-parameter space, the corresponding relations of Ramírez & Meléndez (2005) produce very similar effective temperatures (see Paper I). There are two Alonso et al. calibrations for each index, one suitable for main sequence stars of spectral types F0-K5 (Alonso et al. 1996) and one for giant stars in the same spectral range (Alonso et al. 1999)[4]. Since our targets range from TO stars at the very end of the MS to bRGB stars, both the dwarf and giant calibrations are used to separately derive effective temperatures. Note that by doing so, we also apply the $T_{\rm eff}$ – colour relations to stars that do not fall in the range in colour covered by the calibrations at this metallicity, which may affect the results.

Before applying the calibrations, we eliminate star-to-star scatter caused by errors in the observed colours. We clean the photometric sample based on data quality, as measured by the DAPHOT *SHARP* parameter, and construct fiducial relations between each colour index and the V magnitude, which is the best observed and calibrated quantity. The relations are obtained by averaging the colours for stars in V bins of 0.22 magnitudes. We then shift the observed colour for each star onto the sequence and, finally, we correct all colours for the reddening of NGC 6397. This value has been measured in several studies and typical estimates lie in the range $E(B-V) = 0.17 - 0.20$ (see e.g. Reid & Gizis 1998). Here a value of 0.179 is adopted, following Anthony-Twarog & Twarog (2000). The reddening in the other colour indices are derived from $E(B-V)$, using the relation coefficients given in Ramírez & Meléndez (2005) and $E(v-y) = 1.7 \times E(b-y)$.

Fig. 3 shows a comparison between our derived spectroscopic and photometric effective temperatures for 122 stars (all stars for which the Hα line is observed). The difference between the Hα-based values and the effective temperatures obtained from the dwarf and giant calibrations of the narrow-band index $v-y$ and the broad-band index $V-I$ are plotted against $T_{\rm eff,H\alpha}$. The agreement between Hα and the $v-y$ dwarf calibration scale is good for the hotter half of the sample, with spectroscopic $T_{\rm eff} \geq 5\,900$ K. The average difference for individual stars is here ~ 70 K. For the cooler half, at spectroscopic $T_{\rm eff} \leq 5\,900$ K, good agreement is instead seen with the giant calibration, with a mean difference ~ 50 K. The spectroscopic temperature scale hence suggests a transition between the two $v-y$ calibration scales at some point in the middle of the SGB, in line with what may be expected. The other narrow-band index, $b-y$ (not shown), produces very similar effective temperatures to the $v-y$ scales. The $V-I$ dwarf calibration scale appears similar in relative behaviour to $v-y$, but the effective temperatures are shifted towards slightly cooler values, giving a good agreement with the spectroscopic $T_{\rm eff}$ for the cooler half of the $T_{\rm eff}$-range. The giant scale, however, is evidently too cool overall to reproduce the spectroscopic results. For $B-V$ (not shown) the two Alonso et al. calibrations result in scales that are identical to each other to within 5 K. In comparison to the Hα-based values the agreement is reasonable at the hotter end whereas the cooler end is offset to higher temperatures by up to ~ 200 K. This index thus implies a markedly shorter total effective temperature range for our sample than the other three.

As an additional test, we also compared the effective temperatures obtained with the Alonso et al. relations to $(v-y)$ and $(b-y)$-calibrations based on synthetic MARCS colours (Gustafsson et al. 2008; calibrations to be published in Önehag et al. 2008, in preparation). The theoretical calibrations reproduce the $T_{\rm eff}$-range spanned by the targets well, indicating a somewhat shorter total range, by about ~ 70 K, than what is predicted from a combination of the two Alonso et al. relations for $b-y$ and $v-y$, respectively.

Much effort has previously been made to pin down the effective-temperature scale of this cluster at the SGB. A summary of the results from six high-resolution studies, including Paper I, is given in Fig. 4, along with our spectroscopic and four photometric scales. In the plot, which illustrates visual magnitude versus effective temperature, filled symbols represent previous results, and lines represent this study. For clarity, we show only a smoothed relation between V and $T_{\rm eff,H\alpha}$ (the 1σ-scatter around this line is 90 K) and only parts of the photometric $V-T_{\rm eff}$ relations based on $v-y$ and $V-I$, i.e. the Alonso et al. (1996) calibration is applied only to the hotter half and the Alonso et al. (1999) only to the cooler half of the stellar sample. All data are collected from the stated publications or from references therein. Only the effective temperatures that are actually adopted by the different authors are shown, even if several different scales are presented in the study. The visual magnitudes in the sample of Thévenin et al. (2001) are from their Table 1, taking the average whenever two values are given.

Fig. 4 shows that the different studies agree within approximately 200 – 300 K at a given visual magnitude, which may be a reasonable error, albeit undesirably large when the aim is precise chemical abundances. Most studies focus on TO stars and the only two studies, except the present, that include stars on both ends of the SGB are Paper I and Gratton et al. (2001). On a relative scale, which is most essential for this work, we

[3] http://www.eso.org/observing/dfo/quality/GIRAFFE/pipeline/solar.html

[4] Calibrations for the $v-y$-index for dwarf and giant stars are published in Paper I.

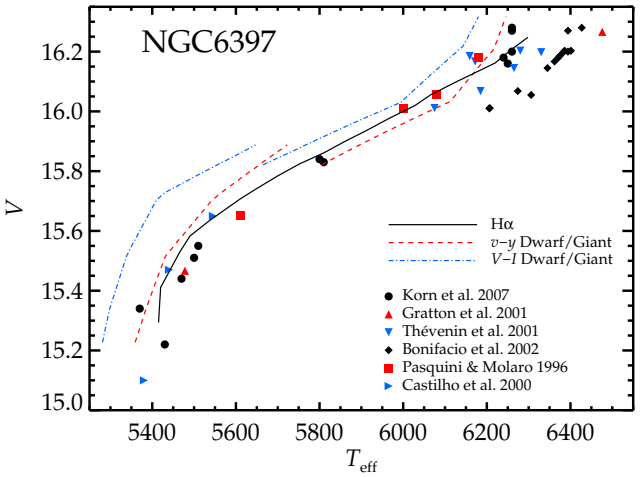


Fig. 4. Comparison between our spectroscopic $T_{\rm eff}$-scale, the photometric values obtained from $v-y$ and $V-I$, and the results from six other studies.

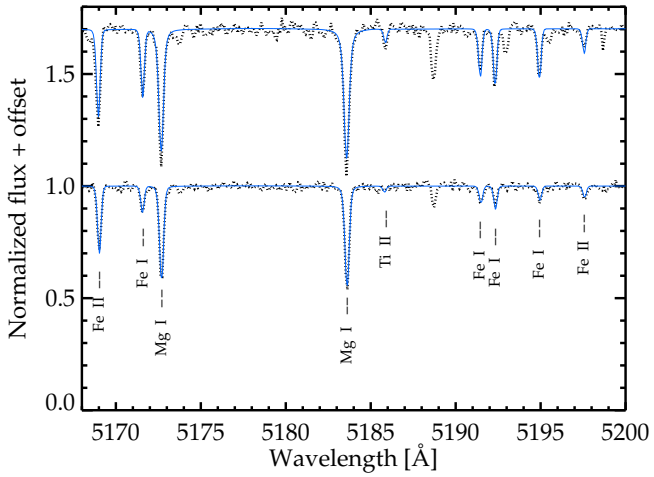


Fig. 5. A selected part of two observed, normalised spectra (dotted lines) and the best fitting model spectra (solid lines), as determined by the analysis code. Note that the models in this figure only contain the spectral lines that are used in the abundance analysis. These lines are marked with labels. The top spectrum belongs to the bRGB star 23267 and the bottom plot to the TO star 12318

predict a slightly larger effective temperature range between $V = 15.5 - 16.2$ than Paper I and a shorter range than Gratton et al. In the former study, effective temperatures are also obtained by Hα profile fitting but using a different model atmosphere and spectrum synthesis code (ODF-MAFAGS, Grupp 2004, Fuhrmann et al. 1993). For the eight targets in common with this study we find group-averaged effective temperatures that are different by less than 10 K. The typical difference for individual stars is 50 K. The $T_{\rm eff}$ value found for the TO-star group of the Gratton et al. study exceeds our estimate by almost 200 K and is extensively discussed in Paper I, where the authors point out that the effective-temperature assignment of Gratton et al. , based on Hα, may be systematically affected by the echelle-order blaze residuals imprinted on the continuum in the UVES (slit-mode) observations. Differences in model atmospheres and hydrogen line-broadening theory used may also explain part of the offset (see Paper I).

3.2. Surface gravities

We derive surface gravities for the target stars using the customary relation between effective temperature, luminosity, mass, and surface gravity. Luminosities are calculated from the apparent visual magnitude V and the Alonso et al. (1999) calibration for bolometric correction, which is given as a function of metallicity, [Fe/H][5], and $T_{\rm eff}$. The metallicity is set to −2.0 for all stars. The distance modulus of NGC 6397 is assumed to be 12.57. Stellar masses are inferred from a 13.5 Gyr isochrone of the cluster (Richard et al. 2005), which places the stars in the mass range $0.78\,M_\odot - 0.79\,M_\odot$. With these values, the surface gravity found for TO stars at $T_{\rm eff} = 6\,250$ K is $\log g = 3.96$ and $\log g = 3.40$ for bRGB stars at $T_{\rm eff} = 5\,450$ K. We use a single, averaged value of $\log g$ for all stars for which we have derived the same $T_{\rm eff}$.
The aim of this study is to draw conclusions about abundance differences between stars. We are therefore mainly interested in the accuracy with which we can determine surface gravities on the relative, rather than the absolute scale. In this respect, the effective temperatures have the largest, albeit small, influence on the surface gravity values. A rise in effective temperature of 100 K corresponds to an increase in logarithmic surface gravity of approximately 0.03 dex. This can be compared to an increase in stellar mass by $0.01\,M_\odot$ that propagates into a rise in $\log g$ by 0.005 dex. We set a constant metallicity, to avoid circular arguments as regards the existence of abundance trends. The influence of [Fe/H] on the derived surface gravities is anyway small. An increase in [Fe/H] by 0.1 dex propagates into a decrease in $\log g$ of 0.006 dex. We estimate the relative error in V to approximately 0.01 magnitudes, which gives a contribution to the error in $\log g$ of 0.004 dex. The value of the distance modulus only affects the absolute values of the surface gravities. An increase in $(m-M)_V$ of 0.5 corresponds to an overall rise in $\log g$ of 0.2 dex. Given these low dependencies of relative photometric surface-gravity values on other parameters, abundance differences within the sample can be constrained from gravity-sensitive lines (e.g. those of Fe II) with high confidence.

3.3. Spectrum analysis code

For abundance analysis of the stellar sample we use the same automated code as developed for the Hamburg/ESO R-process enhanced star survey, (HERES, Barklem et al. 2005). We summarise here some important aspects of the analysis code, referring the reader to Barklem et al. for a full description.
The software is built on the IDL and C++ based Spectroscopy Made Easy (SME) package by Valenti & Piskunov (1996), with subsequent updates, but has been modified to run without any user interaction. Some improvements have also been made to the original SME spectrum synthesis code, most importantly the inclusion of continuous scattering in the source function. As the software is implemented, we supply it with 1) a count spectrum and the measurement error in each pixel, 2) the final stellar parameters $T_{\rm eff}$ and $\log g$ and an initial guess for the metallicity ([Fe/H]= −2.0), 3) a list of lines to base the abundance analysis on and wavelength windows where each line can be found and 4) a grid of MARCS (Asplund et al. 1997) plane-parallel model atmospheres, all with scaled solar abundances except for an enhancement of alpha-elements of 0.4 dex. This setup is the

[5] $[X/Y] = \log\left(\frac{N_X}{N_Y}\right) - \log\left(\frac{N_X}{N_Y}\right)_\odot$ where N_X is the number density of element X.

same as implemented in Barklem et al. (2005), except that we keep $\log g$ fixed.

The code automatically normalises a spectral region stretching 7 Å on both sides of each given wavelength window, by iterative fitting of a low-order polynomial. At this point any remaining cosmic ray hits are also identified and discarded. The line central wavelength is determined and, if necessary, shifted slightly (within the estimated uncertainty) to coincide with the model wavelength. Observed and modelled spectra are then compared and the best statistical match is determined via a parameter-optimization algorithm (Marquardt 1963; Press et al. 1992). We assume the stars to be slow rotators and fix the projected rotational velocity to $1\,\mathrm{km\,s^{-1}}$. The free parameters are thus the abundance, the microturbulence ξ, and the macroturbulence v_{macro} (Gaussian, isotropic), in which also the instrumental broadening is included. The online appendix contains a list of all lines used in the abundance analysis, with references to the gf-values that were adopted. Based on the availability of lines covered in the spectra, we choose to derive abundances of iron, titanium, calcium, and magnesium. Fig. 5 shows a selected part of two observed, normalised spectra and the best-fit model spectra.

The analysis assumes LTE line formation in one-dimensional, plane-parallel, model atmospheres. These simplifying assumptions can, of course, influence the derived abundances to a certain extent, which we discuss further in Sect. 4. In particular, strong line cores are expected to be poorly described by LTE photospheric models. To avoid large biases, pixel values below 50 % of the continuum flux are generally disregarded.

To analyse the resulting abundances, we also need knowledge about how errors in the stellar parameters affect them. By rerunning the code with one perturbed parameter at a time, holding the others fixed, the abundance sensitivity to these quantities are found for the elements considered. We make three such additional runs, with $T_{\mathrm{eff}}+100\,\mathrm{K}$, $\log g+0.3\,\mathrm{dex}$, and $\xi+0.2\,\mathrm{km\,s^{-1}}$.

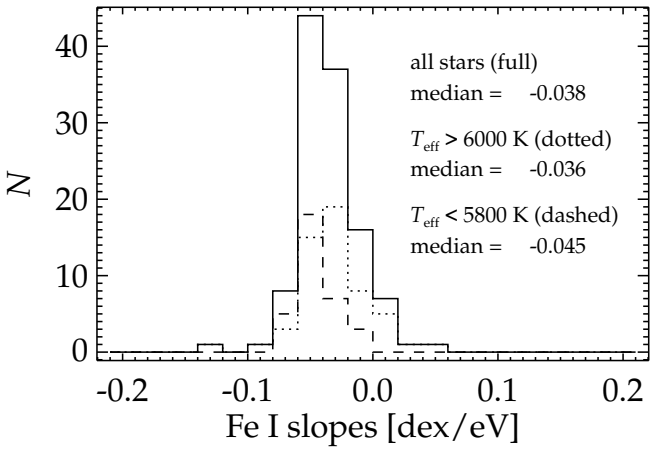


Fig. 6. A histogram of the slopes obtained for linear fits of iron abundance with excitation potential of Fe I lines.

5 450 K and 6 250 K, and the estimated 1σ scatter in $\log\epsilon$[6]. The microturbulence values are found to gradually decrease from a value $1.86 \pm 0.13\,\mathrm{km\,s^{-1}}$ for the stars at $T_{\mathrm{eff}} = 6\,250\,\mathrm{K}$ to $1.47 \pm 0.09\,\mathrm{km\,s^{-1}}$ for the stars at 5 450 K.

A preliminary analysis of the stars found to be non-members based on radial-velocity measurements (see Sect. 2) reveals that they are both subgiants, with approximate stellar parameters $T_{\mathrm{eff}} = 5\,700\,\mathrm{K}$ and $\log g = 3.3$. We find [Fe/H] = −0.6 for 501856 and [Fe/H] = −1.1 for 502219, both indicating [Ca/Fe] = 0.3. Among the cluster stars, 7720 is found to have consistently outlying abundances. With $T_{\mathrm{eff}} = 5\,580\,\mathrm{K}$, it displays abundances exceeding the average by 0.19 – 0.26 dex. The star has excellent agreement between Hα-based and photometry-based effective temperatures and a radial velocity typical of the cluster.

4. Results

Fig. 7 shows our derived chemical abundances of magnesium, calcium, and iron, for 116 stars. Six stars, for which we have only two observations each, were rejected due to largely deviating abundance results (not shown), most likely caused by the low quality of these spectra. General trends are obtained by averaging the abundances in effective-temperature bins of 500 K (with shrinking box-size towards each end) and then applying additional smoothing to avoid the influence from outliers. The thin lines shown in the plot indicate the standard deviations of the trends' residuals. For comparison, Fig. 7 also shows the results from Paper I (open squares). Note that the abundances of Fe, Mg, and Ca then were derived by non-LTE (hereafter NLTE) analysis.

It is evident that our derived abundances indeed suggest that there are trends with effective temperature on the SGB. Especially in iron there is a notable trend of increased abundances towards lower T_{eff}. The magnesium values display a similar behaviour, but due to larger star-to-star scatter the trend is less clearly visible. The calcium abundances may point to a slight, insignificant, increase towards cooler effective temperature, whereas the titanium abundances rather indicate the opposite, equally insignificant, trend with T_{eff}. Table 2 summarises the average abundances we derive for all elements at two representative effective temperature points,

4.1. Error sources

There are several possible sources of error to consider, which may effect our abundances on the relative and absolute scale. First of all our analysis relies on the assumption of LTE line formation, which is not in general a good approximation for metal-poor stars. Particularly lines from neutral minority species are believed to form out of LTE. NLTE corrections are expected to be larger in cool metal-poor stars than in their metal-rich counterparts, mainly because the reduced amount of metals gives less line-blocking in the UV, which causes more over-ionisation. Also, the amount of free electrons available in the atmosphere is reduced in metal-poor stars, which means less LTE-establishing electron collisions. Considering the narrow range in stellar parameter space covered by our targets, we would expect NLTE corrections to be similar for all stars, thereby mainly influencing the abundances on the absolute scale.

The second point we consider is the abundance dependence on stellar parameters, most importantly on effective temperature. Table 3 shows what effect perturbing T_{eff}, $\log g$, and ξ from their derived values has on the derived abundances of all elements, at two effective temperature points. With this knowledge it is easily predicted how systematic errors in e.g. our T_{eff} scale

[6] $\log\epsilon_{\mathrm{x}} = \log\left(\frac{N_{\mathrm{x}}}{N_{\mathrm{H}}}\right) + 12$

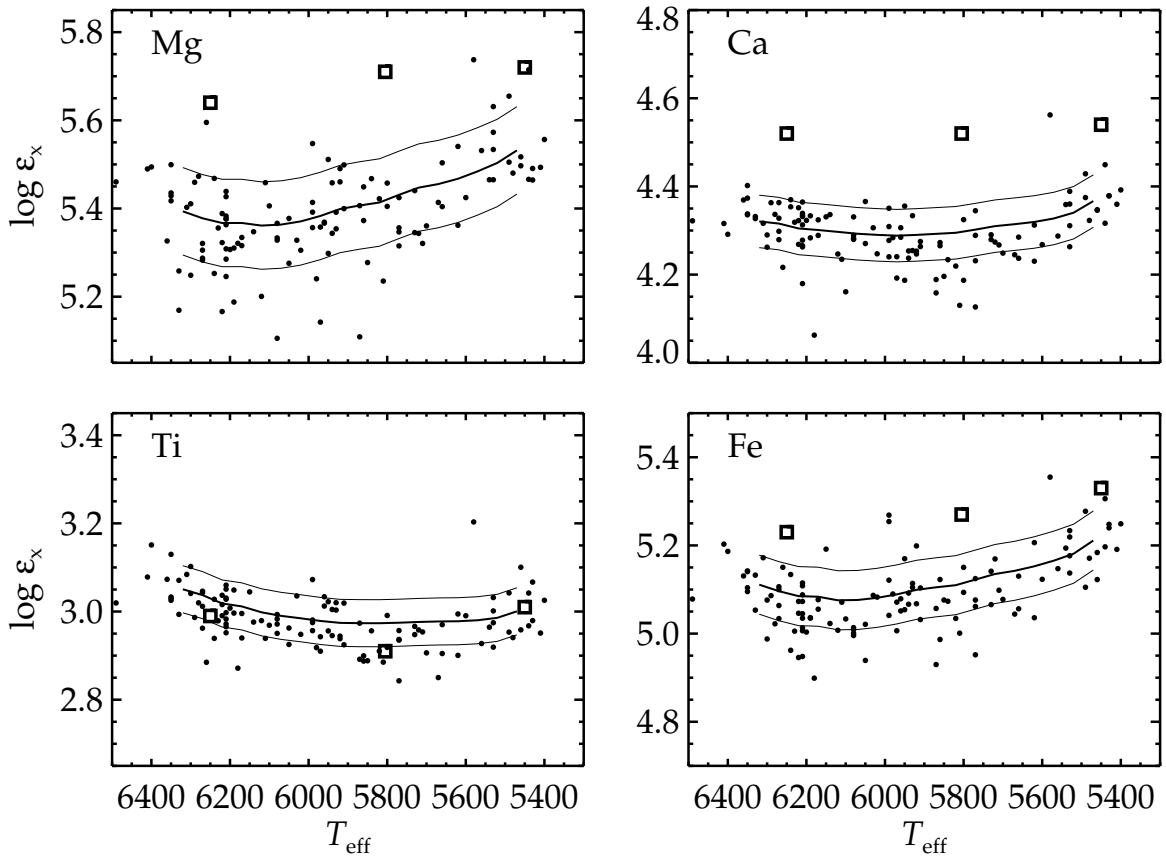


Fig. 7. Abundance trends (filled dots) with effective temperature for Mg, Ca, Ti, and Fe from analysis of 116 stars. The thick lines display general trends and the thin lines show estimated 1σ limits. Open squares represent the results from Paper I, in which Mg, Ca, and Fe are treated in NLTE and Ti in LTE.

Table 2. Average abundances obtained at two effective temperature points.

	$T_{\rm eff}$ [K]	$\log g$ [cgs]	ξ [km s^{-1}]	$\log\epsilon_{\rm Mg}$	$\sigma_{\rm Mg}$	$\log\epsilon_{\rm Ca}$	$\sigma_{\rm Ca}$	$\log\epsilon_{\rm Ti}$	$\sigma_{\rm Ti}$	$\log\epsilon_{\rm Fe}$	$\sigma_{\rm Fe}$
	6 250	3.96	1.86	5.37	0.10	4.31	0.06	3.03	0.05	5.09	0.07
	5 450	3.40	1.47	5.54	0.10	4.38	0.06	3.00	0.05	5.22	0.07
Δ	800	0.56	0.39	−0.17		−0.07		0.03		−0.13	

would influence the results. When discussing this issue for each element, we take into account that changes in the effective temperature scale cause changes in surface gravity (see Sect. 3.2). We neglect possible changes in ξ caused by altering $T_{\rm eff}$ or $\log g$.

The most influential parameter on the chemical abundances is the effective temperature. As seen in Sec. 3.1, $T_{\rm eff}$-determinations based on Hα and cluster photometry seem to be in good agreement, but additional information can be drawn from the excitation equilibria of the targets. Generally, the abundance of each element is the one that gives the optimal match to all lines, but for testing purposes we also compute individual abundances for all neutral iron lines and thus can compare our adopted temperature scale with that implied by excitation equilibrium. The resulting slopes obtained for iron abundance with excitation potential of the lines are shown in a histogram in Figure 6. The median slope for the sample is negative, -0.038 dex/eV, i.e. overall cooler effective temperatures are needed to establish the equilibria. By estimate, the equilibria of the hottest stars, $T_{\rm eff} > 6000$ K, are reproduced with a lowering of the effective temperatures of approximately 270 K. The stars in the cooler half, $T_{\rm eff} < 5800$ K, require a similar change, 260 K, as the abundance slopes with excitation potential are more negative than the hotter half, but also have a higher temperature-sensitivity. There is thus no sign of a sizeable expansion or contraction of the adopted effective-temperature scale.

A third source of error originates in the spectrum itself. We may judge how well GIRAFFE performs in comparison to the higher resolution spectrograph UVES as eight of our observed stars, five TO stars and three bRGB stars, are the same targets as presented in Paper I. The results from measurements of a number of equivalent widths of lines in the GIRAFFE and UVES spectra of these stars are displayed in Fig. 8. The equivalent widths measured in the GIRAFFE spectra are plotted against the corresponding value obtained from the same lines in the UVES spectra. Filled circles represent TO stars and open circles bRGB stars. The results indicate that the GIRAFFE spectra have slightly weaker lines compared to those obtained with UVES. The difference amounts to approximately

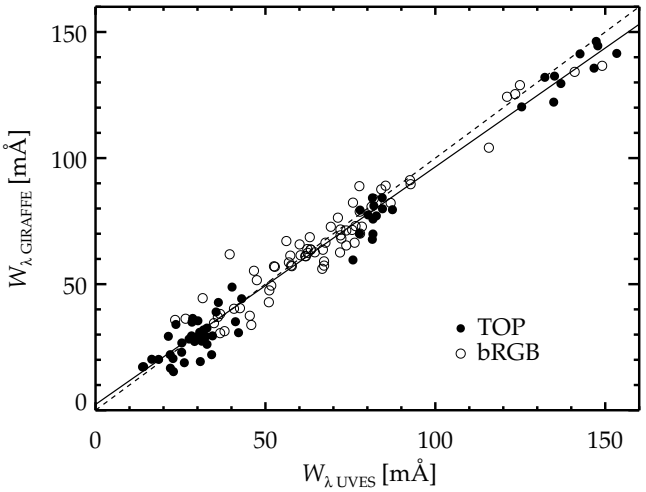


Fig. 8. The figure shows a comparison between equivalent widths measured for the same lines in spectra of the same stars, obtained with GIRAFFE and UVES, respectively. The filled circles corresponds to stars located at the TO and the open circles to bRGB stars. The dashed line mark 1:1 agreement and the solid line is a linear fit to the measurements.

4 %, which in logarithmic abundance units corresponds to −0.02 dex (assuming a linear relation between abundance and equivalent width). There is no obvious difference between TO and bRGB stars, leading us to conclude that this has no impact on the relative abundances we derive for our sample stars.

4.2. Magnesium

Our magnesium abundances are based on two of the Mg Ib triplet lines, 5 172 Å and 5 183 Å. As seen in Table 3, magnesium is the most sensitive of all elements to $T_{\rm eff}$ and $\log g$, which may contribute to explaining the higher level of scatter, approximately 0.10 dex, seen in $\log \epsilon_{\rm Mg}$ compared to the other elements. Another probable source of scatter is conversion of Mg to Al, which is observed as an inverse correlation between the two elements in GC stars (see e.g. Gratton et al. 2004).

As seen in Table 2 we obtain a difference of 0.17 dex between stars at the cooler and hotter end of the SGB. For a trend of this size to vanish, i.e. for our magnesium abundances to agree over the whole sample, the effective temperature of the TO stars would have to be raised by at least 320 K, and more, around 450 K, if one takes into consideration a simultaneous rise in surface gravity of 0.03 dex per 100 K (See Sect. 3.2), since the two stellar parameters have opposite influence on the magnesium abundance. Alternatively, the effective temperature of the bRGB stars would have to be lowered by 170 − 220 K. We note that the trend we obtain of 0.17 dex is larger than the 0.08 dex found in Paper I for the difference in magnesium abundance between their bRGB stars at average $T_{\rm eff}$ = 5 456 K and TO stars at $T_{\rm eff}$ = 6 254 K.

Based on existing studies, NLTE corrections for lines of neutral magnesium are positive in these stars, due to over-ionization. Paper I, following Gehren et al. (2004), calculate $\log \epsilon_{\rm NLTE} - \log \epsilon_{\rm LTE}$ to range between 0.11 dex and 0.14 dex in their sample, based on Mg I 5 528 Å. Hence there are only small differential effects in abundance, judging from this line. Mashonkina et al. (2008) find an average NLTE correction of 0.12 dex for the somewhat hotter, but otherwise very similar, metal-poor star HD 84937, from five Mg I lines, including 5 528 Å, 5 172 Å, and 5 183 Å.

NLTE effects are pronounced in the line cores of the triplet lines, in this case leading to the observed lines being deeper than the LTE-based prediction. These influences are partly avoided for the coolest stars in the sample, for which the line cores extend deeper than 50% of the continuum flux and are disregarded by the spectrum analysis code. In the hottest stars, all pixels contributing to the lines are evaluated. Given this methodology, differential effects on the abundance trend obtained from photospheric NLTE modelling, including the line core, cannot be excluded.

4.3. Calcium

Nine lines of neutral calcium are considered in the determination of $\log \epsilon_{\rm Ca}$. The strongest lines, i.e. those consisting of the highest number of pixels and thereby having the largest influence on the derived abundances, are 4 434 Å, 4 454 Å, 6 462 Å, and 6 439 Å. Our average calcium abundances increase from 4.31 dex at the TO to 4.38 dex at the bRGB, i.e. a trend of 0.07 dex. This can be compared to 0.02 dex found in Paper I, based on 6 122 Å, 6 162 Å, and 6 439 Å. Table 3 shows that $\log \epsilon_{\rm Ca}$ has a low sensitivity to changes in $T_{\rm eff}$ and $\log g$ and the scatter in abundance is also small. To completely remove a trend of 0.07 dex in calcium abundance, one would have to raise the TO star effective temperatures by 500 − 750 K (assuming the dependence is linear also for such a large perturbation), again depending on the corresponding change in surface gravity, or equivalently lower the bRGB star effective temperatures by 210 − 260 K.

Following Mashonkina et al. (2007) we estimate the NLTE corrections to the calcium abundances for the 6 439Å and 4 454Å lines. For the former line, we find a minor abundance correction of +0.05 dex for the TO stars and no correction at all for the bRGB stars, while the latter line points to +0.13 dex at the hotter end and +0.10 dex at the cooler end. We would therefore expect that the trend in calcium abundance resulting from NLTE analysis of these lines is almost flat. Considering the possibility of differential NLTE abundance corrections of this size, it is clear that our inferred trend as such is insignificant.

4.4. Titanium

The titanium abundances are based on twelve Ti II lines and three Ti I lines, all except two (Ti II 5 188 Å and 5 226 Å) situated in the spectral range 4 390 − 4 540 Å. LTE line formation is believed to be a fair approximation for Ti II, since this is the dominant ionization stage. For neutral titanium one would on the other hand not expect LTE to be valid, but no thorough NLTE analysis exists in the literature covering this wavelength range for metal-poor stars. In any case, singly ionised titanium lines dominate neutral ones in our abundance analysis, both in terms of number and line strengths, and we therefore assume NLTE corrections to be of lesser importance.

On the absolute scale, the Ti abundances are in good agreement with the results from Paper I, which are based on Ti II 5 188 Å and 5 226 Å. We obtain abundances ranging from 3.03 dex at 6 250 K to 3.00 dex at 5 450 K, and the abundances from Paper I fall within our 1σ limit of 0.04 dex from these values. The abun-

dance difference we find between TO stars and bRGB stars is −0.03 dex, whereas Paper I report a positive trend of 0.02 dex. Due to the large influence from Ti II lines, $\log \epsilon_{\rm Ti}$ has a positive reaction to a rise in surface gravity contrary to the other elements and is also highly insensitive to changes in effective temperature at the hotter end. Lowering the surface gravity of the TO stars by 0.15 dex, or alternatively raising the bRGB surface gravity by 0.21 dex, would result in a flat trend.

4.5. Iron

We include 51 Fe I lines and 9 Fe II lines in our analysis. Considering that the latter are comparatively weak, we estimate that lines from Fe I bear higher weight. We find a trend of 0.13 dex between TO and bRGB stars, again slightly larger than the 0.10 dex reported in Paper I. The average iron abundance of the sample ranges from 5.09 dex to 5.22 dex, corresponding to [Fe/H] = −2.41 to −2.28, using $\log \epsilon_{\rm Fe,\odot} = 7.5$. To flatten the trend, one would need to raise the TO star $T_{\rm eff}$ by 350 − 390 K or lower $T_{\rm eff}$ at the bRGB by 190 − 230 K. Following Korn et al. (2003), Paper I find a minor NLTE abundance correction for neutral iron at the level of 0.03-0.05 dex in TO stars as well as in RGB stars and practically no differential NLTE effects between the groups. The small size of the corrections is likely due to the adoption of high rates of collisions with neutral hydrogen, and we do not exclude that NLTE corrections may adjust our iron abundances significantly upward.
Neglecting differential NLTE influences and other possible modelling deficits, the significance level of the identified trend in iron abundance depends only on errors in relative stellar parameters. An estimate of the error in $\Delta \log \epsilon_{\rm Fe}$ between TO and bRGB stars can be obtained by adding the individual errors listed in Table 3 in quadrature for the hottest and coolest stars, respectively. Assuming we have constrained the range of the effective-temperature scale to better than 100 K, the surface-gravity scale within 0.1 dex, and the microturbulence scale within 0.1 km s^{-1}, the total error in abundance is 0.050 dex at $T_{\rm eff}$ = 6250 K and 0.080 dex at $T_{\rm eff}$ = 5450 K. A lower limit on the significance of the trend is thus 0.13/0.080 = 1.6 sigma, corresponding to approximately 90%.

4.6. Comparison to other studies

In general our results for the TO stars agree well with the LTE abundances obtained for the sample included in the study by Thévenin et al. (2001), whilst their NLTE values are significantly higher. Taking the average of their LTE values (given in their Table 4) results in abundances that lie up to 0.1 dex above the findings in this work. Similar difference is seen between our iron abundances and the LTE values obtained in Paper I. There is a larger offset, ∼0.15 dex, between the LTE abundances for magnesium and calcium. We estimate that the small differences in stellar parameters between the studies can account for up to 0.1 dex in logarithmic abundance and that the remaining part originates in line selection and modelling techniques. This is confirmed by a re-analysis of two of the UVES targets in Paper I, using the same automated procedure and line list as we have implemented in this study. However, for the discussion of abundance trends, differences in absolute abundance on this level are irrelevant.
Other values reported from medium- or high-resolution spectroscopic studies of NGC 6397 are [Fe/H] = −2.03 ± 0.02 ± 0.04 (Gratton et al. 2001), [Fe/H] = −2.0 ± 0.05 (Castilho et al. 2000), [Fe/H] = −2.21 ± 0.05 (Gratton 1982), −1.88 (Gratton & Ortolani 1989), −1.99 ± 0.01 (Minniti et al. 1993), −1.82 ± 0.04 (Carretta & Gratton 1997). We note that several of the mentioned studies are performed exclusively on giant stars.

Table 3. Sensitivity of logarithmic abundances to stellar parameters.

Element	$T_{\rm eff}$	$T_{\rm eff}$+100 K	log g + 0.1 dex	ξ + 0.1 km s^{-1}
Mg	6 250	0.053	-0.053	-0.048
Mg	5 450	0.097	-0.075	-0.025
Ca	6 250	0.014	-0.016	-0.025
Ca	5 450	0.033	-0.023	-0.032
Ti	6 250	0.001	0.019	-0.029
Ti	5 450	0.014	0.014	-0.036
Fe	6 250	0.037	-0.014	-0.031
Fe	5 450	0.066	-0.025	-0.038

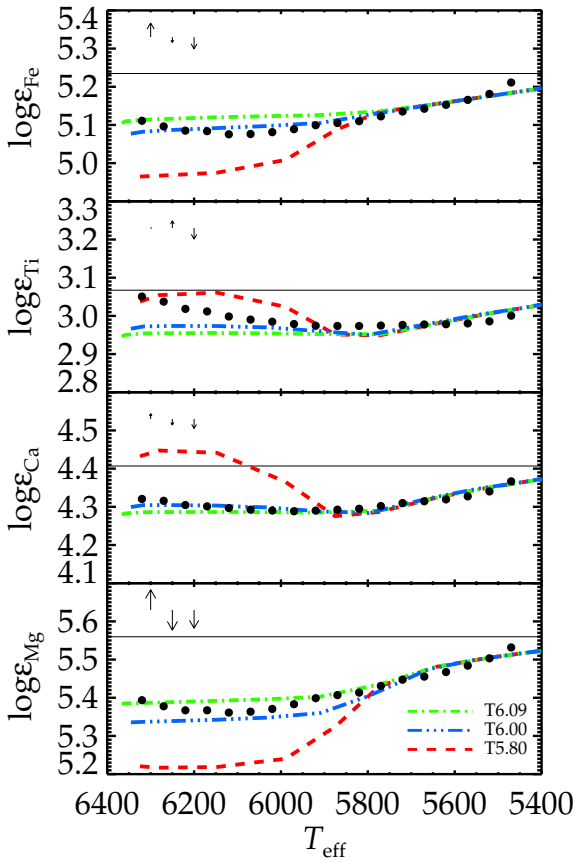


Fig. 9. Comparison between the abundance trends from Fig. 7 (here displayed with black dots) and the predictions from stellar structure models including atomic diffusion and turbulent mixing. The horizontal, black, solid lines represent the initial abundances of the models. The three arrows in the upper left corner of each plot indicate the abundance change at $T_{\rm eff}$ = 6 250 K when raising the effective temperature by 100 K (left), raising the surface gravity by 0.1 dex (middle), and raising the microturbulence values by 0.1 km/s (right).

5. Discussion

Abundance variations in GCs of the kind our analysis suggests may be explained with stellar-structure models that allow for radial diffusion of chemical elements. We compare our obtained abundances to predictions from models of Population II stars by Richard et al. (2002, 2005), which account for all the physics of particle transport that can be modelled from first principles (see Paper I, Richard et al. 2005, and references therein).

The main free parameter in these models is the introduction of turbulent transport of unknown physical nature, which the authors conclude to be best parameterised as a (decreasing) function of temperature and density. Additional mixing is needed to meet the strong observational evidence of a flat and thin plateau of Li in metal-poor TO and SGB stars over a wide range in metallicities, known as the 'Spite plateau' of lithium (Spite & Spite 1982). Omitting turbulent mixing, the plateau cannot be reproduced by the models, as too much Li diffuses into the stellar interior. In Fig. 9 we illustrate the predictions from three models implementing different values of a reference temperature T_0, which controls the efficiency of the mixing. The models are denoted by T5.80 (lowest efficiency), T6.00 (the best fitting efficiency to the results in Paper I), and T6.09 (highest efficiency) and represent the range in least efficient mixing that is compatible with the Spite plateau of lithium. The absolute abundances predicted by the three models are slightly adjusted, individually for each element, to agree with our derived abundances in the cooler half of the effective-temperature range ($\leq$ 5800 K), where the three models coincide. Here, the region mixed by turbulence is fully encompassed by the convective envelope and the mixing efficiency is irrelevant for the surface abundances. The black solid horizontal lines mark the initial abundances of the models (accounting for the vertical shifts), $\log \epsilon_{\rm Mg} = 5.56$, $\log \epsilon_{\rm Ca} = 4.41$, $\log \epsilon_{\rm Ti} = 3.07$, and $\log \epsilon_{\rm Fe} = 5.23$, or [Fe/H] = −2.27.

The comparison shows that the predicted increase in surface abundances from $T_{\rm eff} \approx 5\,800$ K to 5 400 K is overall well reproduced by our obtained values. We further conclude that, within reasonable error bars, the best-fitting model found in Paper I (T6.00) is also a good choice for this sample of stars. Generally, it is clear that the surface iron and magnesium abundances predicted from models including atomic diffusion and mixing are more compatible with the results of our analysis than flat trends are.

6. Conclusions

We have presented a homogeneous analysis of medium-high resolution spectroscopic data covering a large sample of stars, located between the TO point and bRGB of the globular cluster NGC 6397. The obtained iron abundances show a significant trend with evolutionary stage. The magnesium abundances also indicate the presence of a trend of similar size, but the high sensitivity of this element to stellar parameters combined with the possibility of differential NLTE corrections prevent an unambiguous detection. The calcium and titanium abundances can be reconciled with a flat behaviour. The difference in iron abundances between the stars at $T_{\rm eff,H\alpha} = 5\,450$ K and stars at $T_{\rm eff,H\alpha} = 6\,250$ K amounts to 0.13 dex in $\log \epsilon_{\rm Fe}$, a trend that is robust to realistic errors in stellar parameters. Raising the effective temperatures of the hottest stars by $\sim$ 350 K would remove the trend in iron abundance. Considering that the total range in effective temperature between the considered points is 800 K, this would imply an error in our $T_{\rm eff}$-scale of 43 %, which we regard as unlikely. Alternatively, the same effect may be achieved by lowering the effective temperatures of the coolest stars by $\sim$ 200 K, correspoding to a systematic error of almost 25 %. Even that is an improbably large correction, given the good agreement between spectroscopy, through profile-fitting of Hα and the different photometric calibrations that were exploited. The excitation equilibrium of Fe I points to cooler $T_{\rm eff}$-values overall, but on the relative scale the agreement is satisfactory. Overall, the results of this study independently support the conclusions of Korn et al. (2007), indicating that atomic diffusion significantly affects the surface abundances of metal-poor stars near the main turn-off point.

The abundance analysis is based on traditional LTE analysis using 1D, hydrostatic model atmospheres. Although it seems that corrections to the obtained abundances of Fe and Mg by 1D, NLTE modelling have no large differential impact in comparison to the sizes of the found trends, we cannot rule out that our results are artifacts from insufficient modelling techniques. More sophisticated models, implementing NLTE line formation in 3D, dynamical model atmospheres may provide a more definite answer. Some explorations with LTE line formation using 3D models were performed in Paper I, indicating that the results are robust in this respect.

The obtained abundance trends with effective temperature are, for magnesium, calcium, and iron, well reproduced by stellar-structure models including atomic diffusion and turbulent mixing. Especially, the good relative agreement seen at the cooler half of the SGB, where additional turbulent transport is irrelevant, indeed lends support to the notion that atomic diffusion shapes the surface abundances of unevolved metal-poor stars.

Acknowledgements. We thank O. Richard for providing stellar-structure models and A.Önehag for letting us apply a yet unpublished colour-$T_{\rm eff}$ calibration. B. Gustafsson is thanked for valuable discussions and comments to the work. We thank the referee who helped improve the paper. K. L. is grateful to F. Primas and J. Sundqvist for their support and proof-readings of the manuscript. A. J. K. acknowledges research fellowships by the Leopoldina Foundation/Germany (under grant BMBF-LPD 9901/8-87). F. G. acknowledges support from the Danish AsteroSeismology Centre, the Carlsberg Foundation, and the Instrument Center for Danish Astronomy (IDA). P. B. is a Royal Swedish Academy of Sciences Research Fellow supported by a grant from the Knut and Alice Wallenberg Foundation. A. J. K. and P. B. also acknowledge support from the Swedish Research Council. This research has made use of the VizieR catalogue access tool, CDS, Strasbourg, France.

References

Alonso, A., Arribas, S., & Martinez-Roger, C. 1996, A&A, 313, 873
Alonso, A., Arribas, S., & Martínez-Roger, C. 1999, A&AS, 140, 261
Anstee, S. D. & O'Mara, B. J. 1995, MNRAS, 276, 859
Anthony-Twarog, B. J. & Twarog, B. A. 2000, AJ, 120, 3111
Asplund, M., Gustafsson, B., Kiselman, D., & Eriksson, K. 1997, A&A, 318, 521
Bard, A., Kock, A., & Kock, M. 1991, A&A, 248, 315
Barklem, P. S., Christlieb, N., Beers, T. C., et al. 2005, A&A, 439, 129
Barklem, P. S. & Piskunov, N. 2003, in IAU Symposium, Vol. 210, Modelling of Stellar Atmospheres, ed. N. Piskunov, W. W. Weiss, & D. F. Gray, 28P–+
Barklem, P. S., Piskunov, N., & O'Mara, B. J. 2000, A&A, 363, 1091
Barklem, P. S., Stempels, H. C., Allende Prieto, C., et al. 2002, A&A, 385, 951
Biemont, E., Baudoux, M., Kurucz, R. L., Ansbacher, W., & Pinnington, E. H. 1991, A&A, 249, 539
Blackwell, D. E., Menon, S. L. R., Petford, A. D., & Shallis, M. J. 1982, MNRAS, 201, 611
Bonifacio, P., Pasquini, L., Spite, F., et al. 2002, A&A, 390, 91
Carretta, E. & Gratton, R. G. 1997, A&AS, 121, 95
Castilho, B. V., Pasquini, L., Allen, D. M., Barbuy, B., & Molaro, P. 2000, A&A, 361, 92
Fuhrmann, K., Axer, M., & Gehren, T. 1993, A&A, 271, 451
Gehren, T., Liang, Y. C., Shi, J. R., Zhang, H. W., & Zhao, G. 2004, A&A, 413, 1045

Gratton, R., Sneden, C., & Carretta, E. 2004, ARA&A, 42, 385
Gratton, R. G. 1982, A&A, 115, 171
Gratton, R. G., Bonifacio, P., Bragaglia, A., et al. 2001, A&A, 369, 87
Gratton, R. G. & Ortolani, S. 1989, A&A, 211, 41
Grupp, F. 2004, A&A, 420, 289
Gustafsson, B., Bell, R. A., Eriksson, K., & Nordlund, A. 1975, A&A, 42, 407
Gustafsson, B., Edvardsson, B., Eriksson, K., et al. 2008, A&A, 486, 951
Heise, C. & Kock, M. 1990, A&A, 230, 244
Korn, A. J., Grundahl, F., Richard, O., et al. 2007, ApJ, 671, 402 (Paper I)
Korn, A. J., Shi, J., & Gehren, T. 2003, A&A, 407, 691
Kroll, S. & Kock, M. 1987, A&AS, 67, 225
Kurucz, R. L., Furenlid, I., Brault, J., & Testerman, L. 1984, Solar flux atlas from 296 to 1300 nm (National Solar Observatory Atlas, Sunspot, New Mexico: National Solar Observatory, 1984)
Marquardt, D. W. 1963, SIAM Journal on Applied Mathematics, 11, 431
Martin, G. A., Fuhr, J. R., & Wiese, W. L. 1988, Phys. Chem. Ref. Data, 17, 3
Mashonkina, L., Korn, A. J., & Przybilla, N. 2007, A&A, 461, 261
Mashonkina, L., Zhao, G., Gehren, T., et al. 2008, A&A, 478, 529
Milone, A. P., Villanova, S., Bedin, L. R., et al. 2006, A&A, 456, 517
Minniti, D., Geisler, D., Peterson, R. C., & Claria, J. J. 1993, ApJ, 413, 548
Moity, J. 1983, A&AS, 52, 37
O'Brian, T. R., Wickliffe, M. E., Lawler, J. E., Whaling, J. W., & Brault, W. 1991, Journal of the Optical Society of America B Optical Physics, 8, 1185
Ochsenbein, F., Bauer, P., & Marcout, J. 2000, A&AS, 143, 23
Pasquini, L., Avila, G., Blecha, A., et al. 2002, The Messenger, 110, 1
Pasquini, L. & Molaro, P. 1996, A&A, 307, 761
Pickering, J. C., Thorne, A. P., & Perez, R. 2001, ApJS, 132, 403
Piskunov, N. E. 1992, in Stellar Magnetism, ed. Y. V. Glagolevskij & I. I. Romanyuk, 92–+
Press, W. H., Teukolsky, S. A., Vetterling, W. T., & Flannery, B. P. 1992, Numerical recipes in FORTRAN. The art of scientific computing (Cambridge University Press, 2nd ed.)
Ramírez, I. & Meléndez, J. 2005, ApJ, 626, 465
Reid, I. N. & Gizis, J. E. 1998, AJ, 116, 2929
Richard, O., Michaud, G., & Richer, J. 2005, ApJ, 619, 538
Richard, O., Michaud, G., Richer, J., et al. 2002, ApJ, 568, 979
Schnabel, R., Schultz-Johanning, M., & Kock, M. 2004, A&A, 414, 1169
Smith, G. & Oneill, J. A. 1975, A&A, 38, 1
Smith, G. & Raggett, D. S. J. 1981, Journal of Physics B Atomic Molecular Physics, 14, 4015
Spite, M. & Spite, F. 1982, Nature, 297, 483
Stehlé, C. & Hutcheon, R. 1999, A&AS, 140, 93
Thévenin, F., Charbonnel, C., de Freitas Pacheco, J. A., et al. 2001, A&A, 373, 905
Valenti, J. A. & Piskunov, N. 1996, A&AS, 118, 595
Wiese, W. L. & Martin, G. A. 1980, NSRDS-NBS, No 68, Part II

Online Material

Table 4. Stellar parameters and abundances derived for the sample stars. Targets marked with * are the targets of Korn et al. (2007).

ID	α(2000)	δ(2000)	V	$T_{\mathrm{H}\alpha}$ [K]	$\log g$ [cgs]	ξ [km s^{-1}]	$\log \epsilon_{\mathrm{Mg}}$	$\log \epsilon_{\mathrm{Ca}}$	$\log \epsilon_{\mathrm{Ti}}$	$\log \epsilon_{\mathrm{Fe}}$	$v-y$	$T_{v-y,\mathrm{Dwarf}}$ [K]	$T_{v-y,\mathrm{Giant}}$ [K]	$V-I$	$T_{V-I,\mathrm{Dwarf}}$ [K]	$T_{V-I,\mathrm{Giant}}$ [K]
10174	17 40 10.680	53 37 41.30	16.171	6220	3.93	1.86	5.39	4.35	3.02	5.07	0.693	6194	5931	0.583	6105	5941
10197*	17 40 10.770	53 38 26.40	16.160	6190	3.91	1.98	5.19	4.28	3.05	5.04	0.695	6187	5926	0.585	6096	5933
10268	17 40 11.160	53 40 26.20	16.163	6200	3.92	1.83	5.31	4.32	3.01	5.00	0.694	6189	5927	0.585	6098	5935
10372	17 40 11.680	53 44 30.40	15.543	5410	3.31	1.48	5.49	4.36	2.95	5.19	0.892	5541	5448	0.761	5439	5348
10387	17 40 11.480	53 38 45.60	16.113	6080	3.85	1.78	5.33	4.28	2.95	5.01	0.702	6159	5907	0.594	6058	5902
10672	17 40 12.460	53 40 41.60	15.587	5480	3.47	1.53	5.48	4.32	2.94	5.17	0.881	5573	5474	0.755	5457	5365
10676	17 40 12.610	53 43 41.10	16.317	6400	4.06	1.98	5.49	4.29	3.15	5.19	0.680	6246	5965	0.566	6180	6005
10902	17 40 13.340	53 42 39.30	16.060	6080	3.85	1.90	5.11	4.33	2.99	5.00	0.710	6128	5886	0.603	6017	5866
10917	17 40 13.250	53 39 53.80	15.865	5770	3.67	1.60	5.35	4.29	2.94	5.12	0.785	5864	5700	0.675	5733	5616
10976	17 40 13.710	53 45 36.40	15.804	5660	3.61	1.68	5.50	4.29	2.97	5.13	0.810	5782	5639	0.701	5639	5532
11066	17 40 13.710	53 39 15.40	16.238	6350	4.02	1.90	5.42	4.37	3.03	5.14	0.685	6225	5951	0.573	6151	5980
11153	17 40 13.980	53 39 33.40	16.312	6270	3.97	1.88	5.31	4.30	3.01	5.06	0.680	6244	5964	0.567	6178	6003
11318	17 40 14.500	53 38 56.90	15.683	5460	3.44	1.33	5.50	4.35	3.10	5.12	0.856	5644	5531	0.743	5497	5402
11794	17 40 15.840	53 34 36.30	15.940	5940	3.77	1.76	5.34	4.24	2.95	5.07	0.753	5971	5777	0.645	5848	5718
12082	17 40 16.740	53 35 11.70	15.802	5660	3.61	1.56	5.40	4.24	2.90	5.06	0.811	5780	5637	0.702	5636	5529
12318*	17 40 17.640	53 39 34.20	16.182	6210	3.93	1.73	5.38	4.31	3.00	5.11	0.691	6201	5935	0.581	6113	5948
12387	17 40 18.090	53 44 57.50	16.173	6210	3.93	1.73	5.38	4.36	3.03	5.09	0.693	6195	5931	0.583	6106	5942
12473	17 40 18.340	53 44 38.50	16.097	6280	3.97	1.92	5.47	4.34	3.02	5.02	0.704	6150	5901	0.597	6046	5891
12881	17 40 19.640	53 45 23.30	15.980	5990	3.80	1.81	5.36	4.31	2.96	5.12	0.736	6031	5819	0.629	5912	5775
13053	17 40 19.900	53 39 49.00	16.010	6140	3.88	1.83	5.35	4.34	2.98	5.02	0.724	6077	5851	0.617	5961	5818
13093	17 40 20.100	53 41 47.10	16.187	6330	4.01	1.87	5.17	4.33	3.07	5.13	0.690	6204	5937	0.580	6117	5952
13160	17 40 20.350	53 43 18.40	15.821	5700	3.63	1.55	5.36	4.25	2.91	5.08	0.803	5805	5656	0.694	5665	5555
13466	17 40 21.040	53 40 01.20	15.829	5990	3.80	1.77	5.41	4.35	3.07	5.27	0.800	5815	5664	0.690	5677	5566
13535	17 40 21.380	53 43 05.30	15.988	6030	3.82	1.69	5.33	4.31	3.04	5.09	0.733	6043	5828	0.626	5925	5786
13552	17 40 21.360	53 41 43.40	16.043	6110	3.87	1.66	5.46	4.23	2.94	5.07	0.713	6118	5880	0.607	6004	5855
13683	17 40 21.800	53 43 56.60	15.776	5620	3.58	1.66	5.36	4.23	2.90	5.04	0.822	5747	5611	0.713	5597	5494
13885	17 40 22.050	53 37 54.10	15.906	5800	3.69	1.68	5.46	4.19	2.92	5.09	0.768	5922	5742	0.659	5795	5672
13909	17 40 22.000	53 35 22.20	15.956	5980	3.79	1.83	5.24	4.28	2.92	5.09	0.747	5995	5794	0.639	5873	5741
14522	17 40 24.050	53 44 26.50	16.207	6210	3.93	1.87	5.31	4.33	2.95	5.01	0.687	6216	5945	0.577	6134	5966
14589	17 40 24.120	53 42 36.40	16.089	6170	3.90	1.86	5.32	4.32	3.00	5.08	0.706	6145	5898	0.598	6040	5885
15344	17 40 25.740	53 35 20.90	15.890	5910	3.75	1.70	5.50	4.28	2.92	5.10	0.774	5899	5725	0.665	5770	5650
15957	17 40 27.430	53 36 53.80	16.287	6350	4.02	2.01	5.43	4.40	3.03	5.10	0.682	6238	5959	0.569	6169	5995
16588	17 40 29.010	53 37 42.30	15.837	5800	3.69	1.74	5.40	4.32	2.99	5.15	0.797	5826	5671	0.687	5689	5578
16792	17 40 29.880	53 44 49.70	15.956	5930	3.76	1.56	5.39	4.33	3.02	5.10	0.747	5995	5794	0.639	5873	5741
16822	17 40 29.600	53 37 38.40	15.860	5670	3.61	1.62	5.41	4.24	2.85	5.04	0.787	5857	5695	0.677	5725	5610
17100	17 40 30.610	53 43 52.70	16.002	6050	3.83	1.76	5.28	4.37	2.96	5.02	0.727	6064	5843	0.620	5948	5806
17167	17 40 30.770	53 44 01.20	16.014	6150	3.89	1.74	4.97	4.33	3.04	5.19	0.722	6083	5856	0.615	5968	5823
17629	17 40 31.520	53 37 03.30	15.779	5720	3.64	1.61	5.34	4.27	2.96	5.17	0.820	5750	5614	0.712	5602	5498
17841	17 40 31.980	53 36 38.00	15.764	5600	3.57	1.44	5.42	4.27	2.99	5.12	0.827	5731	5600	0.718	5580	5478
17925	17 40 32.130	53 35 56.30	16.295	6300	3.99	2.22	5.25	4.26	3.10	4.99	0.681	6240	5961	0.568	6172	5998
17964	17 40 32.620	53 43 41.70	16.037	6210	3.93	1.71	5.44	4.26	2.98	5.05	0.714	6115	5877	0.608	5999	5851
18670	17 40 33.980	53 37 14.90	16.297	6310	3.99	1.66	5.40	4.32	3.08	5.17	0.681	6240	5961	0.568	6173	5999
18866	17 40 34.320	53 35 54.20	15.888	5770	3.67	1.70	5.36	4.34	2.96	5.08	0.775	5896	5723	0.666	5767	5647
20071	17 40 37.160	53 37 29.50	15.551	5440	3.39	1.60	5.71	4.45	3.04	5.31	0.890	5547	5452	0.760	5442	5351
23267*	17 40 43.750	53 37 17.40	15.339	5430	3.36	1.60	5.46	4.38	2.98	5.25	0.920	5466	5385	0.778	5386	5298
2978	17 39 37.960	53 40 53.10	15.935	5810	3.70	1.70	5.24	4.13	2.89	5.00	0.755	5964	5772	0.647	5840	5712
3124	17 39 38.870	53 38 07.20	16.136	6190	3.91	1.88	5.31	4.33	3.00	5.04	0.698	6173	5917	0.590	6077	5917

ID	α(2000)	δ(2000)	V	$T_{\mathrm{H}\alpha}$ [K]	log g [cgs]	ξ [km s^{-1}]	log ϵ_{Mg}	log ϵ_{Ca}	log ϵ_{Ti}	log ϵ_{Fe}	$v-y$	$T_{v-y,\mathrm{Dwarf}}$ [K]	$T_{v-y,\mathrm{Giant}}$ [K]	$V-I$	$T_{V-I,\mathrm{Dwarf}}$ [K]	$T_{V-I,\mathrm{Giant}}$ [K]
3296	17 39 39.840	53 37 07.30	15.619	5460	3.44	1.32	5.52	4.35	2.96	5.18	0.873	5596	5493	0.751	5471	5377
3602	17 39 41.630	53 34 56.90	15.981	5840	3.71	1.65	5.47	4.23	2.96	5.07	0.736	6032	5821	0.628	5913	5776
3796	17 39 42.980	53 39 25.30	16.231	6210	3.93	1.68	5.25	4.18	2.97	5.03	0.686	6223	5950	0.573	6148	5978
3838	17 39 43.220	53 38 59.40	16.292	6210	3.93	1.79	5.29	4.27	3.05	4.95	0.681	6239	5960	0.568	6171	5997
3867	17 39 43.290	53 35 09.50	15.743	5490	3.48	1.36	5.51	4.37	2.95	5.11	0.835	5705	5579	0.727	5549	5450
3892	17 39 43.720	53 40 50.60	15.966	5870	3.73	1.50	5.41	4.19	2.97	5.06	0.742	6010	5805	0.635	5889	5755
4114	17 39 44.760	53 39 46.50	16.263	6300	3.99	1.98	5.41	4.29	3.04	5.08	0.683	6231	5955	0.571	6160	5988
500199	17 40 22.870	53 31 56.40	15.621	5540	3.52	1.50	5.47	4.36	2.96	5.19	0.872	5597	5494	0.751	5471	5378
500645	17 39 40.890	53 32 55.80	16.264	6210	3.93	1.78	5.36	4.28	2.97	5.01	0.683	6232	5955	0.571	6160	5988
500725	17 39 47.550	53 33 03.70	16.013	5960	3.78	1.45	5.37	4.28	3.03	5.05	0.723	6081	5855	0.616	5966	5822
500949*	17 40 34.580	53 33 20.70	15.514	5440	3.39	1.57	5.47	4.32	2.97	5.20	0.900	5520	5431	0.764	5428	5338
501164	17 39 45.530	53 33 48.60	15.906	6050	3.83	1.87	5.38	4.27	2.93	4.94	0.768	5922	5742	0.659	5795	5672
501236	17 40 28.760	53 33 55.70	16.213	6270	3.97	1.98	5.28	4.33	2.96	5.03	0.687	6218	5946	0.576	6139	5970
501262	17 40 32.860	53 33 58.40	16.137	6210	3.93	1.89	5.43	4.34	3.06	5.11	0.698	6174	5917	0.589	6077	5918
501368	17 40 31.820	53 34 14.30	16.180	6270	3.97	1.92	5.29	4.36	3.05	5.10	0.691	6199	5934	0.582	6112	5947
501389	17 40 45.430	53 34 17.50	16.197	6270	3.97	1.96	5.32	4.28	3.04	5.11	0.689	6210	5941	0.578	6126	5959
501939	17 39 22.590	53 35 52.70	16.049	6080	3.85	1.76	5.33	4.29	2.97	5.01	0.712	6122	5882	0.605	6009	5859
502286	17 40 46.740	53 36 49.10	16.016	6260	3.96	1.78	5.60	4.22	2.88	5.15	0.721	6086	5858	0.614	5971	5826
502729	17 39 22.140	53 38 23.40	15.831	5730	3.65	1.56	5.35	4.29	2.95	5.14	0.799	5818	5665	0.689	5680	5569
502740	17 39 10.480	53 38 25.90	15.607	5430	3.36	1.27	5.49	4.38	3.07	5.24	0.876	5587	5486	0.752	5465	5373
502882	17 39 22.740	53 38 51.90	15.801	5530	3.51	1.44	5.63	4.26	2.92	5.14	0.811	5779	5636	0.702	5635	5528
504920	17 40 37.920	53 44 02.80	15.898	5990	3.80	1.55	5.55	4.28	2.98	5.25	0.771	5910	5734	0.662	5783	5661
505031	17 40 37.050	53 44 17.70	15.770	5920	3.76	1.88	5.49	4.25	2.94	5.20	0.824	5739	5606	0.716	5588	5486
505253	17 40 41.730	53 44 40.90	15.923	5950	3.77	1.82	5.51	4.36	3.02	5.17	0.760	5946	5760	0.652	5821	5695
505471	17 40 36.670	53 45 02.80	16.122	6490	4.12	2.06	5.46	4.32	3.02	5.08	0.700	6165	5911	0.592	6065	5908
505513	17 40 42.670	53 45 05.60	16.226	6290	3.98	1.99	5.46	4.36	2.99	5.09	0.686	6221	5949	0.574	6146	5976
505913	17 40 22.730	53 45 37.30	15.928	5860	3.73	1.60	5.45	4.27	2.89	5.12	0.758	5953	5765	0.650	5829	5702
506120*	17 40 41.590	53 45 49.30	16.271	6220	3.93	2.27	5.17	4.27	2.99	4.95	0.683	6233	5957	0.570	6163	5990
506139	17 40 31.030	53 45 51.80	15.834	5940	3.77	1.68	5.46	4.25	3.00	5.09	0.798	5822	5668	0.688	5685	5573
507010	17 40 42.060	53 46 45.70	15.248	5400	3.29	1.54	5.56	4.39	3.03	5.25	0.930	5441	5364	0.783	5370	5284
507031	17 40 36.410	53 46 47.70	16.048	6180	3.91	1.77	5.32	4.06	2.87	4.90	0.712	6121	5882	0.606	6008	5858
507433*	17 40 16.070	53 47 18.60	16.278	6350	4.02	1.82	5.44	4.34	3.13	5.14	0.682	6235	5958	0.570	6166	5993
507860	17 40 33.610	53 47 52.40	16.238	6240	3.95	1.46	5.47	4.35	2.94	4.96	0.685	6225	5951	0.573	6151	5980
508219	17 40 17.200	53 48 24.40	16.285	6350	4.02	1.74	5.50	4.34	3.03	5.10	0.682	6237	5959	0.569	6168	5995
5734	17 39 52.820	53 37 03.00	16.148	6120	3.87	1.70	5.20	4.25	2.98	5.01	0.696	6180	5921	0.587	6086	5925
6114	17 39 54.710	53 37 40.20	15.947	5770	3.67	1.60	5.32	4.13	2.84	4.95	0.750	5981	5785	0.642	5859	5728
6119	17 39 54.910	53 42 24.20	16.171	6210	3.93	1.75	5.38	4.33	3.03	5.07	0.693	6194	5931	0.583	6105	5941
6391*	17 39 55.900	53 35 11.90	15.551	5530	3.51	1.61	5.47	4.39	3.03	5.23	0.890	5547	5452	0.760	5442	5351
6550	17 39 56.790	53 40 29.90	15.954	5990	3.80	1.78	5.39	4.24	2.98	5.04	0.747	5992	5792	0.639	5870	5738
6760	17 39 57.710	53 38 39.50	15.832	5710	3.64	1.53	5.32	4.27	2.95	5.10	0.799	5819	5666	0.689	5682	5571
6997	17 39 58.900	53 43 16.10	15.976	5970	3.79	1.69	5.36	4.24	2.94	5.07	0.738	6025	5815	0.630	5905	5769
7081	17 39 59.050	53 38 04.50	15.984	5860	3.73	1.72	5.37	4.27	2.90	4.99	0.735	6037	5824	0.627	5918	5780
7090	17 39 59.350	53 44 36.10	16.164	6100	3.86	1.61	5.41	4.16	2.97	5.03	0.694	6190	5928	0.585	6099	5936
7181	17 39 59.450	53 38 38.30	15.582	5490	3.48	1.46	5.65	4.43	3.04	5.28	0.882	5569	5471	0.756	5455	5363
7512	17 40 00.780	53 35 35.10	15.944	5950	3.77	1.92	5.30	4.19	2.96	5.05	0.752	5977	5782	0.643	5854	5724
7599	17 40 01.210	53 37 52.70	16.073	6170	3.90	1.86	5.33	4.29	2.94	5.06	0.708	6136	5892	0.601	6027	5875
7611	17 40 01.520	53 43 46.80	15.932	5770	3.67	1.59	5.42	4.23	2.94	5.06	0.757	5959	5769	0.648	5835	5707
7698	17 40 01.580	53 36 49.30	15.703	5620	3.58	1.61	5.54	4.31	2.99	5.21	0.851	5659	5543	0.740	5506	5410
7720	17 40 01.820	53 40 55.00	15.728	5580	3.55	1.39	5.74	4.56	3.20	5.35	0.841	5687	5565	0.733	5528	5430

ID	α(2000)	δ(2000)	V	$T_{\mathrm{H}\alpha}$ [K]	$\log g$ [cgs]	ξ [km s^{-1}]	$\log \epsilon_{\mathrm{Mg}}$	$\log \epsilon_{\mathrm{Ca}}$	$\log \epsilon_{\mathrm{Ti}}$	$\log \epsilon_{\mathrm{Fe}}$	$v-y$	$T_{v-y,\mathrm{Dwarf}}$ [K]	$T_{v-y,\mathrm{Giant}}$ [K]	$V-I$	$T_{V-I,\mathrm{Dwarf}}$ [K]	$T_{V-I,\mathrm{Giant}}$ [K]
8075	17 40 02.960	53 35 35.60	15.923	5820	3.70	1.54	5.42	4.22	2.91	5.03	0.760	5946	5760	0.652	5821	5695
8087	17 40 03.320	53 42 46.80	16.229	6360	4.03	1.59	5.33	4.37	3.07	5.13	0.686	6222	5949	0.574	6147	5977
8099	17 40 03.120	53 36 46.90	15.651	5530	3.51	1.45	5.57	4.31	3.00	5.18	0.864	5620	5512	0.747	5484	5390
8171	17 40 03.760	53 45 09.40	16.243	6410	4.06	1.76	5.49	4.32	3.08	5.20	0.685	6226	5952	0.572	6153	5982
8320	17 40 04.330	53 43 05.80	16.027	6020	3.81	1.67	5.31	4.25	2.95	5.08	0.717	6103	5870	0.610	5989	5842
8344	17 40 04.310	53 39 30.30	15.971	5960	3.78	1.57	5.37	4.31	3.01	5.08	0.740	6017	5810	0.633	5897	5762
8395	17 40 04.770	53 45 30.60	15.981	5970	3.79	1.59	5.14	4.19	2.91	5.01	0.736	6032	5821	0.628	5913	5776
8511	17 40 04.940	53 40 24.70	15.653	5560	3.54	1.66	5.53	4.29	2.93	5.15	0.864	5621	5513	0.746	5485	5391
8598	17 40 05.430	53 44 10.30	16.160	6220	3.93	2.15	5.32	4.32	3.04	5.05	0.695	6187	5926	0.585	6096	5933
8661	17 40 05.430	53 38 19.80	16.119	6240	3.95	1.83	5.25	4.37	3.03	5.13	0.701	6163	5910	0.593	6063	5906
8802	17 40 06.100	53 42 24.40	15.951	5920	3.76	1.83	5.46	4.25	2.94	5.07	0.749	5987	5789	0.641	5865	5734
8848	17 40 06.390	53 45 36.00	16.032	5870	3.73	1.72	5.11	4.16	2.89	4.93	0.715	6111	5875	0.609	5996	5847
8870	17 40 06.350	53 42 09.00	15.973	5930	3.76	1.79	5.35	4.25	3.00	5.11	0.739	6020	5812	0.632	5900	5765
8901	17 40 06.150	53 34 36.50	15.820	5730	3.65	1.68	5.44	4.28	2.97	5.07	0.804	5803	5655	0.694	5663	5554
9173	17 40 07.490	53 44 47.50	16.117	6080	3.85	1.71	5.37	4.28	2.98	5.00	0.701	6162	5909	0.593	6062	5904
9226	17 40 07.200	53 34 59.90	16.225	6230	3.94	1.99	5.36	4.32	2.98	5.01	0.686	6221	5949	0.574	6146	5976
9461	17 40 08.400	53 42 51.60	15.934	5850	3.72	1.67	5.28	4.20	2.89	5.08	0.756	5962	5771	0.647	5838	5710
9483	17 40 08.420	53 41 35.10	15.568	5530	3.51	1.59	5.53	4.36	2.97	5.22	0.886	5559	5462	0.757	5449	5358
9655	17 40 09.090	53 43 26.40	16.200	6330	4.01	2.12	5.26	4.33	2.99	5.05	0.688	6212	5942	0.578	6128	5961
9909*	17 40 09.530	53 34 26.10	15.947	5910	3.75	1.63	5.40	4.26	3.02	5.03	0.750	5981	5785	0.642	5859	5728

Table 5. List of lines used in the abundance analysis, with references to the oscillator strengths used. The columns Waals., Stark., and Rad. list the van der Waals, Stark, and radiative damping data (for a description of the data sources, see Barklem et al. 2005, section 3.2, paragraph 5). Rad. is the logarithm (base 10) of the FWHM given in rad s^{-1}. Non-zero values of Stark. and negative values of Waals. represent the logarithm of FWHM per unit pertuber number density at 10 000 K, given in rad $s^{-1}cm^{-3}$. Positive values of the van der Waals parameter correspond to the notation of Anstee & O'Mara (1995), where a packed parameter is used for the broadening cross-section (σ) for collisions by neutral hydrogen at 10km s^{-1} and its velocity dependence (α). E.g. for the Mg I 5172.684Å line, Waals. = 729.238 means $\sigma = 729$ in atomic units and $\alpha = 0.238$. $d\lambda_{blue}$ and $d\lambda_{red}$ give the extent of the spectral windows used for fitting of each line, blue-wards and red-wards of the central wavelength. Zero values in both columns indicate that the line-contribution is considered in the same window as the one listed directly above.

Ion	λ [Å]	χ [eV]	log gf	Ref.	Waals.	Stark.	Rad.	$d\lambda_{blue}$ [mÅ]	$d\lambda_{red}$ [mÅ]
Mg I	5172.684	2.712	-0.380	1	729.238	0.	7.990	-700	700
Mg I	5183.604	2.717	-0.160	1	729.238	0.	7.990	-700	700
Ca I	4434.957	1.886	-0.007	2	-7.162	-5.602	8.021	-300	100
Ca I	4435.679	1.886	-0.517	2	-7.163	-5.610	8.025	-300	300
Ca I	4454.779	1.899	0.258	2	-7.162	-5.596	8.017	-100	100
Ca I	4455.887	1.899	-0.518	2	-7.162	-5.602	8.021	-300	300
Ca I	5261.704	2.521	-0.579	3	-7.416	-5.756	7.903	-300	200
Ca I	5265.556	2.523	-0.113	3	-7.416	-5.755	7.903	-300	50
Ca I	6439.075	2.526	0.390	3	-7.704	-6.072	7.649	-300	300
Ca I	6462.567	2.523	0.262	3	-7.704	-6.072	7.645	-300	50
Ca I	6493.781	2.521	-0.109	3	-7.704	-6.071	7.640	-300	300
Ti I	4533.241	0.848	0.476	4	-7.593	-5.144	8.083	-300	300
Ti I	4534.776	0.836	0.280	4	-7.596	-5.313	8.079	-300	300
Ti I	4535.568	0.826	0.161	5	-7.840	-5.403	8.079	-300	50
Ti II	4394.059	1.221	-1.780	6	-7.944	-6.601	8.471	-100	300
Ti II	4395.840	1.243	-1.930	6	-7.904	-6.550	8.471	-200	200
Ti II	4399.765	1.237	-1.190	6	-7.946	-6.612	8.461	-300	200
Ti II	4417.714	1.165	-1.190	6	-7.926	-6.665	8.225	-300	300
Ti II	4443.801	1.080	-0.720	6	-7.923	-6.509	8.199	-200	300
Ti II	4450.482	1.084	-1.520	6	-7.920	-6.502	8.199	-300	200
Ti II	4468.507	1.131	-0.600	7	-7.931	-6.723	8.207	-300	300
Ti II	4470.853	1.165	-2.020	6	-7.928	-6.713	8.217	-250	150
Ti II	4501.270	1.116	-0.770	6	-7.931	-6.729	8.199	-300	300
Ti II	4533.960	1.237	-0.530	6	-7.960	-6.661	8.225	-300	100
Ti II	5185.902	1.893	-1.490	6	-7.908	-6.533	8.367	-300	300
Ti II	5226.538	1.566	-1.260	6	-7.953	-6.713	8.217	-300	70
Fe I	4375.930	0.000	-3.031	9	215.249	-6.320	4.622	-150	300
Fe I	4375.986	3.047	-2.029	8	-7.800	-5.760	7.810	0	0
Fe I	4383.545	1.485	0.208	9	295.265	-6.200	7.936	-300	300
Fe I	4404.750	1.557	-0.147	9	301.263	-6.200	7.969	-250	200
Fe I	4415.123	1.608	-0.621	9	308.257	-6.200	7.986	-150	200
Fe I	4427.310	0.052	-2.924	9	-7.880	-6.320	4.696	-100	300
Fe I	4430.614	2.223	-1.728	9	431.302	-6.080	8.606	-250	250
Fe I	4442.339	2.198	-1.228	9	424.302	-6.080	8.599	-300	300
Fe I	4443.194	2.858	-1.043	9	224.263	-6.340	7.799	-150	250
Fe I	4443.196	3.071	-1.905	8	-7.770	-6.020	8.010	0	0
Fe I	4447.717	2.223	-1.339	9	429.302	-6.080	8.604	-250	200
Fe I	4461.653	0.087	-3.210	7	-7.799	-6.320	4.638	-200	200
Fe I	4476.019	2.845	-0.819	9	-7.830	-6.170	7.825	-300	300
Fe I	4476.076	3.686	-0.175	8	-7.670	-4.730	7.935	0	0
Fe I	4482.170	0.110	-3.501	7	-7.799	-6.320	4.529	0	0
Fe I	4482.253	2.223	-1.482	9	-7.788	-6.080	8.599	0	0
Fe I	4489.739	0.121	-3.899	9	218.249	-6.320	4.403	-300	200
Fe I	4494.563	2.198	-1.143	9	416.302	-6.080	8.600	-300	300
Fe I	4528.614	2.176	-0.887	9	407.301	-6.080	8.607	-100	300
Fe I	4531.148	1.485	-2.155	7	-7.678	-6.200	8.083	-250	300
Fe I	4736.773	3.211	-0.752	9	820.231	-5.290	7.798	-200	200
Fe I	4871.318	2.865	-0.363	9	748.235	-5.490	8.005	-300	300
Fe I	4872.138	2.882	-0.567	9	754.235	-5.490	8.004	-300	300
Fe I	4890.755	2.875	-0.394	9	758.236	-5.240	8.004	-350	300
Fe I	4891.492	2.851	-0.112	9	750.237	-5.490	8.009	-300	350

Table 5. Continued.

Ion	λ [Å]	χ [eV]	log gf	Ref.	Waals.	Stark.	Rad.	d$\lambda_{\rm blue}$ [mÅ]	d$\lambda_{\rm red}$ [mÅ]
Fe I	4903.310	2.882	-0.926	9	-7.259	-5.490	8.004	-300	300
Fe I	4918.994	2.865	-0.342	9	750.237	-5.490	8.009	-350	350
Fe I	4918.954	4.154	-0.635	8	-7.510	-4.690	8.470	0	0
Fe I	4920.503	2.832	0.068	9	739.238	-5.490	8.009	-300	300
Fe I	5150.840	0.990	-3.037	9	-7.742	-6.250	7.180	-300	300
Fe I	5166.282	0.000	-4.123	9	-7.826	-6.330	3.540	-180	180
Fe I	5171.596	1.485	-1.721	9	-7.687	-6.200	6.330	-220	220
Fe I	5191.455	3.038	-0.551	9	-7.258	-5.490	8.004	-300	300
Fe I	5192.344	2.998	-0.421	9	-7.266	-5.490	8.010	-300	250
Fe I	5194.942	1.557	-2.021	9	-7.680	-6.200	6.290	-300	200
Fe I	5202.336	2.176	-1.838	7	-7.603	-6.180	8.230	-250	250
Fe I	5202.256	4.256	-0.837	8	-7.765	-6.010	8.320	0	0
Fe I	5216.274	1.608	-2.082	9	-7.674	-6.200	6.220	-300	300
Fe I	5232.940	2.940	-0.058	9	-7.280	-5.490	8.009	-300	300
Fe I	5266.554	2.998	-0.386	9	-7.273	-5.489	8.009	-300	300
Fe I	5269.537	0.859	-1.321	7	-7.761	-6.300	7.185	-350	300
Fe I	5281.790	3.038	-0.834	9	-7.266	-5.490	8.010	-200	200
Fe I	5283.621	3.241	-0.524	9	-7.221	-5.450	7.880	-50	250
Fe I	5324.191	3.211	-0.103	10	-7.235	-5.500	7.880	-250	250
Fe I	5328.039	0.915	-1.466	7	-7.757	-6.302	7.161	-300	150
Fe I	5328.532	1.557	-1.850	9	-7.686	-6.228	6.848	-150	300
Fe I	5339.929	3.266	-0.647	10	-7.221	-5.451	7.874	-250	250
Fe I	6393.601	2.433	-1.576	9	-7.622	-6.310	7.970	-250	250
Fe I	6400.001	3.602	-0.290	10	-7.232	-5.500	7.900	-250	200
Fe I	6430.846	2.176	-1.946	9	-7.704	-6.190	8.220	-220	220
Fe I	6494.981	2.404	-1.273	7	-7.629	-6.330	7.936	-300	300
Fe II	4416.828	2.778	-2.540	11	-7.950	-6.670	8.614	-200	300
Fe II	4491.405	2.856	-2.700	12	-7.950	-6.600	8.481	-200	200
Fe II	4508.288	2.856	-2.312	13	-7.950	-6.670	8.617	-250	250
Fe II	4515.343	2.844	-2.362	14	-7.950	-6.600	8.487	-200	200
Fe II	4923.927	2.891	-1.206	14	-7.914	-6.583	8.489	-300	300
Fe II	5197.577	3.230	-2.100	12	-7.824	-6.600	8.480	-200	200
Fe II	5234.625	3.221	-2.270	15	-7.946	-6.600	8.490	-200	200
Fe II	5284.109	2.891	-3.130	11	-7.914	-6.600	8.530	-160	160
Fe II	5316.615	3.153	-1.850	12	-7.950	-6.600	8.480	-300	100

[1] Wiese & Martin (1980)
[2] Smith & O'Neill (1975)
[3] Smith & Raggett (1981)
[4] Blackwell et al (1982)
[5] R. Kurucz, http://cfaku5.cfa.harvard.edu/ATOMS/2200
[6] Pickering et al (2001)
[7] Martin et al. (1988)
[8] R. Kurucz, http://cfaku5.cfa.harvard.edu/ATOMS/2600
[9] O'Brian et al. (1991)
[10] Bard et al. (1991)
[11] Moity (1983)
[12] Kroll & Kock (1987)
[13] Biemont et al. (1991)
[14] Schnabel et al (2004)
[15] Heise & Kock (1990)